A membrane finite element for fast simulation of overlapping beads geometry during direct energy deposition additive manufacturing

Eric Feulvarch, Alain Rassineux, Jean-Christophe Roux, Alexey Sova, Cedric Pouvreau, François Josse

Noname manuscript No.
(will be inserted by the editor)

A membrane finite element for fast simulation of overlapping beads geometry during direct energy deposition additive manufacturing

Eric Feulvarch · Alain Rassineux · Jean-Christophe Roux · Alexey Sova · Cédric Pouvreau · François Josse

Received: date / Accepted: date

Abstract The aim of this paper is to propose a fast FEM strategy for simulating molten metal deposition geometry during additive manufacturing for studying the influence of the sequence of deposition on the geometry. The approach is inspired by the algorithm initially proposed by Feulvarch *et al.* [Eur. J. of Mech. / A 89 (2021) 104290] for coatings. In this article, the membrane finite element is notably improved and extended for simulating of a large stack of deposits in order to study the building of 3D geometries. A constant vertical evolution rate of the surface tension is introduced to adjust the geometry of the free surface of the molten pool which depends on the hydrodynamics of

Eric Feulvarch
Univ. Lyon, Ecole Centrale de Lyon, LTDS, UMR 5513 CNRS, 58 rue Jean Parot, 42023 Saint-Etienne cedex 02, France
E-mail: eric.feulvarch@enise.ec-lyon.fr

Alain Rassineux
Laboratoire Roberval, Université de Technologie de Compiègne, Centre de Recherche Royallieu ,CS 60319, 60203 Compiègne Cedex, France
E-mail: alain.rassineux@utc.fr

Jean-Christophe Roux
Univ. Lyon, Ecole Centrale de Lyon, LTDS, UMR 5513 CNRS, 58 rue Jean Parot, 42023 Saint-Etienne cedex 02, France
E-mail: jean-christophe.roux@enise.ec-lyon.fr

Alexey Sova
Univ. Lyon, Ecole Centrale de Lyon, LTDS, UMR 5513 CNRS, 58 rue Jean Parot, 42023 Saint-Etienne cedex 02, France
E-mail: alexey.sova@enise.ec-lyon.fr

Cédric Pouvreau
Univ Bretagne Sud, IRDL UMR 6612 CNRS, Centre de Recherche, Rue de St Maude, 56100 Lorient, France
E-mail: cedric.pouvreau@univ-ubs.fr

François Josse
ARQUUS, 15 bis Allée des Marronniers, 78000 Versailles, France
E-mail: jossefrancois56@gmail.com

the liquid phase. The simulation is very fast because it is carried out on a 2D mesh composed of linear triangles that corresponds to the sole free surface of the liquid phase at each time step. Moreover, the implicit nonlinear algorithm developed has the advantage of avoiding matrix systems resolution (reduced RAM memory, efficient parallel computing). In addition, a simple and robust remeshing procedure is detailed in order to avoid too large distortions of the triangular elements during the 'inflating' stage of the workpiece. Its interest lies in the fact that it does not require any field projection typically employed in remeshing procedures, as the geometry serves as the only historical data required to resume FEM computations following each remeshing step. Examples are proposed to clearly evidence the efficiency and robustness of the method developed in terms of geometry and CPU time.

Keywords Simulation · Direct Energy Deposition · Surface tension · Additive manufacturing

1 Introduction

The numerical modeling of metal deposition is a complex problem that involves mass transfer, heat transfer and stress balance in solid and liquid phases. As far as the geometry of the deposit is concerned, it depends on the shape of the free surface of the liquid, especially during the solidification stage at the rear of the molten pool. Therefore, the hydrodynamics of the weld pool must be carefully taken into account for simulating the final geometry, especially the consequences of the Marangoni's effect and buoyancy forces. In litterature, several authors simulated the thermo-fluid couplings in the molten pool during welding or additive manufacturing processes. One can cite Rabier *et al.* [1], Zhang *et al.* [2], Cadiou *et al.* [3] and Saadlaoui *et al.* [4] but the CPU times are always very high for a few seconds of real time of deposition. This is mainly due to the thin discretization in space and time required for modeling the transient phenomena such as the motion of the boundary between the liquid and the solid phases. As an example, Jia *et al.* [5] used a relatively small time step of $5.10^{-5}s$ by applying an implicit (backward) Euler algorithm for time integration. The simulations focus on the treatment of the liquid phase at the scale of the molten pool and they are not applied to the building of a complete workpiece in 3D that would involve a very long CPU time.

The objective of this paper is to propose a fast FEM strategy for simulating molten deposition geometry produced during additive manufacturing. The focus is on accurately replicating the geometry induced by the shape of the molten zone at the scale of an entire workpiece, without considering residual stress and distortion at the moment. The proposed approach is inspired by the algorithm initially published by Feulvarch *et al.* [6] for coatings. Experience shows that this approach is well suited for modeling a low number of overlapping deposits but it is not able simulating satisfactory the shape of a large stack of deposits. For this purpose, the membrane finite element formulation is notably improved and extended for simulating of a large stack of deposits in

order to study the building of 3D geometries. A constant vertical evolution rate of the surface tension is introduced to adjust the geometry of the free surface of the molten pool which depends on the hydrodynamics induced by buoyancy forces and the Marangoni's effect. It is to be noted that the evolution rate of the surface tension is not directly determined from the process parameters. It is calibrated from experimental observations in terms of shape or dimensions of elementary depositions because it depends on numerous parameters such as the chemical composition of the material, the laser power distribution, the orientation of the powder jets, the recoil pressure at high temperature, etc.

The simulation achieves significant computational efficiency by utilizing a 2D mesh composed of linear triangles that dynamically represents the evolving free surface of the liquid phase at each time step. The implicit nonlinear resolution algorithm employed in this work avoids matrix systems resolution to further enhance computational efficiency. In addition, a simple and robust remeshing procedure is detailed in order to avoid too large distortions of the triangular elements during the 'inflating' stage of the workpiece. The interest of this approach lies in the fact that it does not require any field projection typically employed in remeshing procedures, as the geometry serves as the only historical data needed to resume FEM computations following each remeshing step.

Section 2 of this paper is dedicated to the physical modeling. In Section 3, the new numerical formulation is detailed. In section 4, examples are proposed to evidence the efficiency and robustness of the method developed in terms of geometry and CPU time.

2 Theory

2.1 Physical modeling

During additive manufacturing, the material is fed into the molten pool with a powder jet as shown in Fig. 1. The objective is here to model the geometry evolution of the deposition by means of the volume flux balance through the free surface of the molten pool denoted S. The powder deposition rate is defined by means of the volume flux $\mathcal{Q}$ in Eq.(1). It corresponds to the volume of material per unit time gained by the molten zone through its free surface. It is to be noted that $\mathcal{Q}$ does not correspond to the volume of powder sprayed. This is due to multiple collisions in the powder jet that induce the ejection of some particles out of the molten pool. This phenomenon is taken into account by means of the efficiency coefficient η as follows:

$$\mathcal{Q} = \eta \int_S -\mathbf{n} \cdot \mathbf{q}\left(\mathbf{x}, t\right) \, ds \tag{1}$$

where $\mathbf{q}\left(\mathbf{x}, t\right)$ is the powder volume flux per unit surface sprayed downward which depends on the position $\mathbf{x}$ and the time t. $\mathbf{n}$ is the local normalized normal vector to the surface S exiting the molten zone (see Fig. 1). Its orientation

is opposite to the one of the vector $\mathbf{q}(\mathbf{x}, t)$.

During the transient deposition of material, the created 3D geometry progresses following the evolution of the surface S of the molten zone. The geometry of this surface is here assumed as being mainly driven by the curvature effect of the surface tension. From the physicists point of view [7], such an effect is equivalent to that of a tight membrane stuck onto the surface of the molten pool subjected to the surface tension γ and the normal load due to the overpressure in the liquid phase denoted Δp.

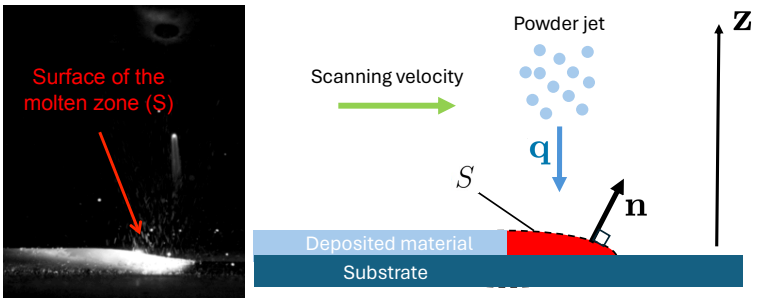

Fig. 1 Longitudinal visualization of the powder sprayed during the LMD-p (Laser Metal Deposition - powder) process.

Fig. 2 shows the effect of the membrane curvature on the equilibrium of a portion of elementary length $ds = 2\,\alpha\,R$ of the membrane in 2D. The force $\Delta p\,\mathbf{n}\,ds$ due to the overpressure in the molten pool opposes to the normal force induced by the surface tension: $\gamma\,\mathbf{t}_1 + \gamma\,\mathbf{t}_2 = -2\,\alpha\,\gamma\,\mathbf{n}$. It is to be noted that this corresponds to the 2D form of the Laplace's law $\Delta p = \gamma\left(\frac{1}{R_1} + \frac{1}{R_2}\right)$ where $\left(\frac{1}{R_1} + \frac{1}{R_2}\right)$ denotes the curvature in 3D. In 2D, we get $R_1 = R$ and $R_2 = +\infty$.

From the numerical point of view, the calculation of the curvature demands an evaluation of the second spatial derivatives of the surface. This requires the use of finite elements of class $\mathcal{C}^1$ [1,8] which are complex to remesh because the modification of the discretization must keep not only of the coordinates but also of their second spatial derivatives.

2.2 Principle of virtual power

In order to avoid the calculation of the curvature, the mechanical impact of γ can be taken into account by means of the virtual power $\mathcal{P}_{int}$ associated to the internal tension of the membrane [7,9–12]:

$$\mathcal{P}_{int} = -\int_S \delta\boldsymbol{D} : (\boldsymbol{I}\,\gamma)\; ds \tag{2}$$

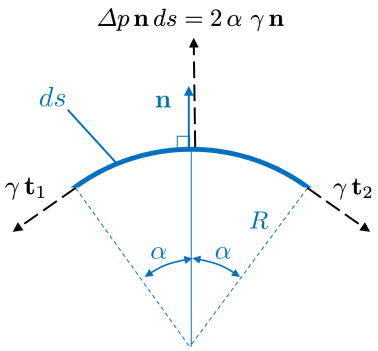

Fig. 2 Curvature effect of the surface tension in 2D.

where $\delta \boldsymbol{D}$ is the symmetric part of the surface gradient of the virtual velocity $\delta \mathbf{v}$ of the membrane; $\boldsymbol{I}$ corresponds to the local surface unit tensor :

$$\boldsymbol{I} = \begin{pmatrix} 1 & 0 \\ 0 & 1 \end{pmatrix} \tag{3}$$

The advantage of modeling the membrane tension in this way lies in the fact that the formulation does not involve the second spatial derivatives of the geometry. Indeed, Eq. (2) only requires the calculation of the gradient of the virtual velocity field i.e. the evaluation of first spatial derivatives. Thus, it is possible to use finite elements of class $\mathcal{C}^0$ without paying particular attention to the transfer of curvature during a remeshing step. Regarding the mechanical equilibrium of the membrane, we propose to express the virtual power $\mathcal{P}_{ext}$ due to the overpressure in the liquid phase as follows:

$$\mathcal{P}_{ext} = \int_S \delta \mathbf{v} \cdot (\Delta p\,\mathbf{n})\; ds \tag{4}$$

As a consequence, the application of the principle of virtual power for the membrane can be written as follows:

$$\forall \delta \mathbf{v}\,,\; \int_S \delta \mathbf{v} \cdot (\Delta p\,\mathbf{n})\; ds - \int_S \delta \boldsymbol{D} : (\boldsymbol{I}\,\gamma)\; ds = 0 \tag{5}$$

with $\delta \mathbf{v} = \mathbf{0}$ on the boundary of the membrane S with the surface of the solid metal around the molten pool.

2.3 The molten pool hydrodynamics

Δp is assumed to play a major role on the geometry of the liquid free surface S. In this work, Δp is not calculated from the fluid flow in the molten pool as would seem natural. We propose to introduce a linear variation of Δp according

to the vertical coordinate denoted z corresponding to the direction of gravity forces (see Fig. 1) :

$$\Delta p = \Delta \overline{p} + \beta\, z \tag{6}$$

where $\Delta \overline{p}$ and β are assumed to be constant on the whole surface S.

As far as the LMD process is concerned, β allows introducing a linear distribution of the overpressure Δp and therefore, an evolution of the curvature as illustrated in Fig. 3. If the value of β is negative, the overpressure Δp decreases when z increases and consequently, so does the curvature. Conversely, a positive value of β leads to an increase in overpressure with z and therefore in curvature. In this way, the influence of the molten pool hydrodynamics can be taken into account on the shape of the free surface without simulating the liquid phase. It is to be noted that the fluid flow depends on buoyancy forces and the "Marangoni" effect that are induced respectively by the temperature dependences of the mass per unit volume and the surface tension. Therefore, the sole parameter β allows modeling implicitly these physical phenomena in a simple manner.

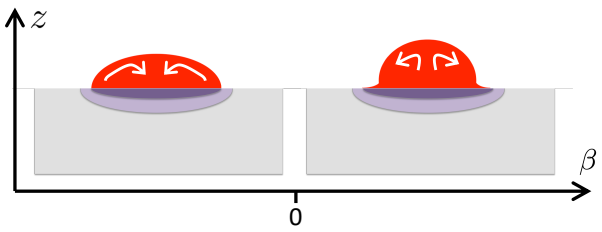

Fig. 3 Influence of β on the transversal shape of a metal deposition (see Eq. 6).

By considering Eq. (6), we get the following form of the principle of virtual power for modeling the geometry of the molten pool surface :

$$\forall \delta \mathbf{v}\,, \int_S \delta \mathbf{v} \cdot (\Delta \overline{p} + \beta\, z)\ \mathbf{n}\, ds - \int_S \delta \boldsymbol{D} : (\boldsymbol{I}\, \gamma)\ ds = 0 \tag{7}$$

From the experimental point of view, the measurement of the surface tension is a very complex challenge. As mentioned above, the influence of its variation with temperature is already accounted for in Eq. (7) with β. Thus, the paramter γ can be assumed to be constant on the surface S and it can be eliminated of all the terms of Eq. (7) as follows:

$$\forall \delta \mathbf{v}\,, \int_S \delta \mathbf{v} \cdot (\Delta \overline{p}^* + \beta^*\, z)\ \mathbf{n}\, ds - \int_S \delta \boldsymbol{D} : \boldsymbol{I}\, ds = 0 \tag{8}$$

where $\Delta\overline{p}^* = \Delta\overline{p}/\gamma$ is a scalar parameter depending on the geometry of the membrane S; $\beta^* = \beta/\gamma$ appears as a global parameter to be calibrated from the shape observed experimentally for a set of deposition parameters (power of laser, flow of powder, deposition velocity...).

The interest of this formulation lies in the fact that it only requires knowledge of the ratio β^* between the surface tension and its supposed constant rate of vertical evolution.

3 Finite element modeling

3.1 Discretization

The numerical modeling is based on a 2D mesh made of linear triangles that inflates in 3D according to the metal deposition trajectory defined by $\mathbf{q}(\mathbf{x}, t) \neq 0$ (see Fig. 1). The geometry of the membrane S is computed in order to satisfy the discrete form of Eq. (8) with a constant value of $\Delta\overline{p}^*$.

Following the usual finite element procedure, Eq. (8) is applied to the function $\delta\mathbf{v}$ of the form:

$$\delta\mathbf{v} = \sum_{i=1}^{N} N_i \, \delta\mathbf{v}_i \tag{9}$$

where $\delta\mathbf{v}_i$ denotes the value of $\delta\mathbf{v}$ at the node numbered i; N_i is the basis function associated with node i; N is the number of nodes belonging to the surface S. Substituting the nodal approximation (9) into Eq. (8), we obtain the following discrete equation for each node belonging to the surface S:

$$\int_S N_i \, (\Delta\overline{p}^* + \beta^* \, z) \, \mathbf{n} \, ds - \int_S \mathbf{B}_i \, ds = 0 \tag{10}$$

where the matrix $\mathbf{B}_i$ is of the following form in each linear triangle e:

$$\mathbf{B}_i^{(e)} = \begin{pmatrix} \frac{\partial N_i}{\partial x_1^{(e)}} \\ \frac{\partial N_i}{\partial x_2^{(e)}} \end{pmatrix} \tag{11}$$

where $x_1^{(e)}$ and $x_2^{(e)}$ denote the coordinates in the local 2D reference frame associated to the finite element e. In order to improve the computation efficiency, the lumping technique [13,14] is applied for the calculation of the first term:

$$(\Delta\overline{p}_i^* + \beta^* \, z_i) \, \mathbf{n}_i \int_S N_i \, ds - \int_S \mathbf{B}_i \, ds = 0 \tag{12}$$

where $\Delta\overline{p}_i^*$ and z_i are the values of $\Delta\overline{p}^*$ and z at node i; $\mathbf{n}_i$ is the nodal normal vector taken equal to the normalized average one :

$$\mathbf{n}_i = \frac{\sum_{e \in E_i} \mathbf{n}^{(e)}}{|| \sum_{e \in E_i} \mathbf{n}^{(e)} ||} \tag{13}$$

where E_i denotes the set of triangles which are adjacent to node i.

The lumping allows multiplying nodal Eq. (12) by $\mathbf{n}_i$ for calculating efficiently $\Delta\overline{p}_i^*$ as a function of the parameter β^* and the geometry of adjacent triangles to node i:

$$\Delta\overline{p}_i^* = \mathbf{n}_i \frac{\displaystyle\int_S \mathbf{B}_i \, ds}{\displaystyle\int_S N_i \, ds} - \beta^* \, z_i \tag{14}$$

3.2 Resolution procedure

At each time step $t + \Delta t$, the simulation consists in first activating the nodes with coordinates $\mathbf{x}_i$ belonging to the surface $S^{(0)}$ defined by $\mathbf{q}(\mathbf{x}_i^{(0)}, t + \Delta t) \neq 0$ (see Eq. (1)) on the geometry of the previous time step. The others are considered as quiet nodes with nil displacements.

Then, the gain of volume is applied on the activated nodes for building $S^{(1)}$ as follows :

$$\mathbf{x}_i^{(1)} = \mathbf{x}_i^{(0)} - \eta \left(\mathbf{q}\left(\mathbf{x}_i^{(0)}, t + \Delta t\right) \mathbf{n}_i^{(0)} \right) \mathbf{n}_i^{(0)} \, \Delta t \tag{15}$$

The membrane geometry is updated in a second stage by means of an iterative procedure in order to satisfy Eq. (10) for all the N activated nodes. For $k > 0$, the nodal values $\Delta\overline{p}_i^{*(k)}$ are first evaluated on the surface $S^{(k)}$ according to Eq. (14). The average one denoted $\Delta\overline{p}^{*(k)}$ is then computed as follows :

$$\Delta\overline{p}^{*(k)} = \frac{\displaystyle\sum_{i=1}^{N} \Delta\overline{p}_i^{*(k)} \int_{S^{(k)}} N_i \, ds}{\displaystyle\sum_{i=1}^{N} \int_{S^{(k)}} N_i \, ds} \tag{16}$$

The geometry of the membrane is considered as being acceptable if the difference $|\Delta\overline{p}^{*(k)} - \Delta\overline{p}_i^{*(k)}|$ is lower than ϵ in a relative way:

$$\max_i \left| \frac{\Delta\overline{p}^{*(k)} - \Delta\overline{p}_i^{*(k)}}{\Delta\overline{p}^{*(k)}} \right| < \epsilon \tag{17}$$

If it is not, the geometry is updated as follows:

$$\mathbf{x}_i^{(k+1)} = \mathbf{x}_i^{(k)} + \lambda^{(k)} \left(\Delta\overline{p}^{*(k)} - \Delta\overline{p}_i^{*(k)} \right) \mathbf{n}_i^{(k)} \tag{18}$$

with

$$\lambda^{(k)} = \min_i \left(\int_{S^{(k)}} N_i \, ds \right)^{\frac{3}{2}} \tag{19}$$

Remark 1 It is to be noted that the explicit correction of the geometry given by Eq.(18) does not affect the initial volume gain computed with Eq.(15) because the volume passing through the surface $S^{(k)}$ can be evaluated in the following way at each iteration :

$$\sum_{i}^{N} \int_{S^{(k)}} N_i \left(\mathbf{x}_i^{(k+1)} - \mathbf{x}_i^{(k)} \right) \mathbf{n}_i^{(k)} \, ds = \lambda^{(k)} \sum_{i}^{N} \int_{S^{(k)}} N_i \left(\Delta \overline{p}^{*(k)} - \Delta \overline{p}_i^{*(k)} \right) ds \tag{20}$$

with

$$\begin{aligned} & \sum_{i}^{N} \int_{S^{(k)}} N_i \left(\Delta \overline{p}^{*(k)} - \Delta \overline{p}_i^{*(k)} \right) ds \\ & = \Delta \overline{p}^{*(k)} \sum_{i}^{N} \int_{S^{(k)}} N_i \, ds - \sum_{i}^{N} \left(\Delta \overline{p}_i^{*(k)} \int_{S^{(k)}} N_i \, ds \right) \\ & = 0 \end{aligned} \tag{21}$$

in accordance with Eq.(16).

Remark 2 The proposed expression of λ is slightly simplified compared to the one initially proposed by Feulvarch *et al.* [6]. The interest of this modification lies in the fact that it decreases the number of iterations at each simulation time step. This increase in the convergence rate is strongly amplified by updating λ at each iteration k with $S^{(k)}$ and not retaining the value calculated with $S^{(1)}$.

3.3 Remeshing procedure

During the 'inflating' stage of the manufactured component, the simulation developed requires a remeshing procedure in order to avoid too large distortions of the triangular elements located in the deposition area always surrounded by the rest of the undeformed 2D mesh. The applied remeshing process is based on standard topological operations, which involves remeshing a set of elements sharing a common edge (swapping, splitting) or the nodes of an edge (mesh coarsening). Remeshing occurs if the new configuration of elements improves the "quality" of the mesh that is determined by the quality criterion of the worst element. Remeshing is performed according to a geometric element quality criterion ξ that depends on the ratio of the inscribed circle radius R_i to the longest edge length h_{max} and a size criterion c [15]:

$$\xi = \frac{R_i}{h_{max}} \, c \tag{22}$$

The objective is to avoid the creation of degenerate elements by controlling the size to maintain sufficient computational precision. It is assumed that a mesh of constant size, h, is desirable. At first, we identify edges whose size exceeds 1.5 times this target size. Then, we perform the remeshing of each element by cutting edges with a simple marching triangles technique inspired

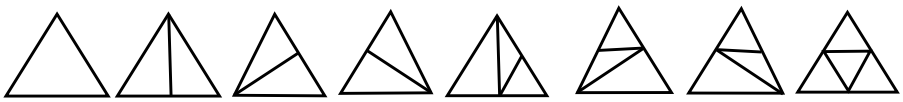

Fig. 4 Marching triangles technique : 8 configurations.

by marching squares [16]. The remeshing configurations for 0, 1, 2, or 3 cut edges are plotted in Fig. 4.

During the cutting stage, small edges may be created. The next step involves deleting "small edges" with a size less than $0.3^{*}h$ as shown in Fig. 5 [15,17]. Only the internal edges (connected to 2 triangles) are modified by merging the two nodes of this edge to form only one as shown in Fig. 5. It is important to note that with the threshold values for cutting (1.5) and mesh coarsening (0.3), no spurious loops are created, and the adaptation process converges. In a second step, the geometric quality of the elements is improved by the technique of edge diagonal inversion as shown in Fig. 5.

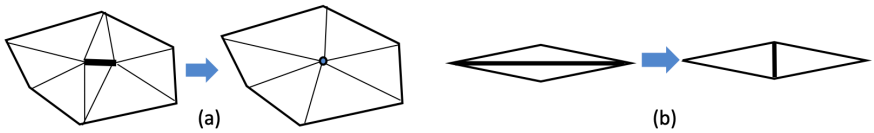

Fig. 5 (a) : Edge collapsing. (b) : Edge swapping.

All these steps are repeated, and the process stops once the mesh is no longer modified. Generally, less than 5 iterations are required. The computational cost of all these operations is very low. The new nodes are created at the midpoints of existing edges. It has been deemed unnecessary to project the midpoint nodes onto an approximate geometry [15], as this would result in significantly higher remeshing costs. Moreover, no Laplacian smoothing of nodes is applied to avoid modifying the geometry.

4 Applications

4.1 Influence of β^{*} on the shape of a single metal deposition

The studied application consists of the deposition of one bead on a plane surface. The distribution of the effective source $\eta\,\mathbf{q}$ (see Eq. (1)) directly depends on the distribution of energy which is assumed to be nearly constant:

$$\eta\,\mathbf{q} = \begin{cases} -\eta\,q_{max}\,\mathbf{z} & \text{if } r < R \\ 0 & \text{otherwise.} \end{cases} \tag{23}$$

where **z** is the ascending vertical axis perpendicular to the horizontal surface of the substrate (see Fig. 1); r denotes the distance to the vertical axis of the source of radius R. The modeling parameters are summarized in Tab. 1. All the simulations have been performed using the software Sysweld® [18] on a laptop computer (Intel(R) Core(TM) i7-10850H CPU @ 2.70Ghz with RAM of 16 Gb).

Scanning velocity	R	$\eta\, q_{max}$	β^*	Δt	ϵ
16.66mm.s^{-1}	2.65mm	3.6mm.s^{-1}	-1 to 1mm^{-2}	0.01s	5%

Table 1 Simulation parameters.

Fig. 6 shows the impact of β^* (ratio between the surface tension and its supposed constant rate of vertical evolution) on the shape of the deposition for a mesh size h equal to 0.3mm without remeshing. The number of iterations never exceeds 7 per time step and the CPU time is lower than 32s for a deposition duration of 5s. As described in section 2.3, one can observe that β^*=1mm^{-2} leads to a thicker deposition than β^*=-1mm^{-2} that tends to broaden the bead through its thickness.

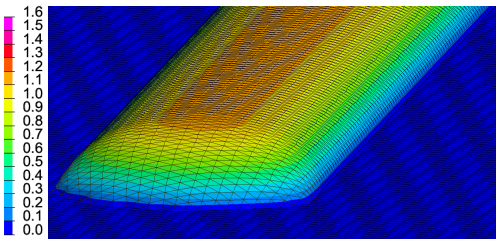

(a) β^*=−1 mm^{-2}

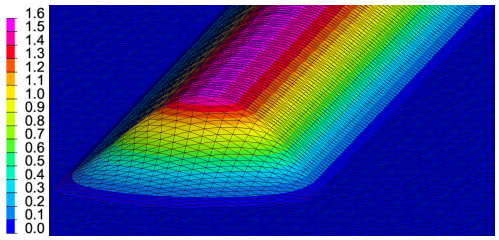

(b) β^*=1 mm^{-2}

Fig. 6 Influence of β^* on the vertical displacement (mm) of the mesh after deposition.

Fig. 7 shows that the change from −1mm^{-2} to 1mm^{-2} can produce an increase of the thickness of the bead by about 33%. The case β^*=0mm^{-2} corresponds to the modeling proposed by Feulvarch *et al.* [6]. One can note that the mesh size h does not significantly influence the final geometry. Moreover,

the contact angle on each side of the deposition is not always the same. This is due to the fact that the nodes on each side are always quiet and the contact angle is a result of the motion of nodes activated during the deposition. It depends on the shape and the size of the mesh.

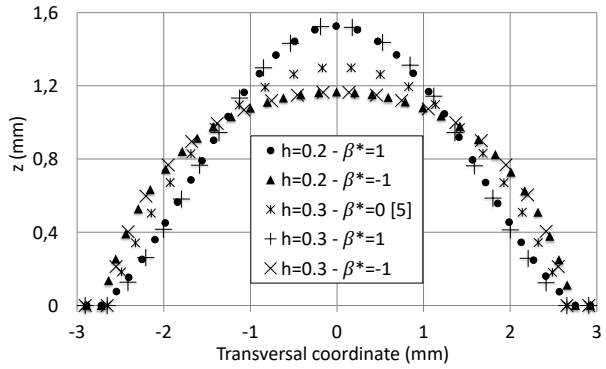

Fig. 7 Bead shape as a function of the mesh size h(mm) and β^*(mm^{-2}).

For comparison, the area under each curve in Fig. 7 is evaluated in Tab. 2 using the trapezoidal rule to analyse the volume gained in the transversal section. It should be noted that the difference between the calculated values never exceeds 1% (see Tab. 3) and it seems to be mainly due to the size of the mesh even if β^* has a significant impact on the final shape of the deposit. In practice, β^* can be calibrated by means of experimental observations or the local multiphysyical simulation of the weld pool [5].

h=0.2 - β^*=1	h=0.2 - β^*=-1	h=0.3 - β^*=0 [5]	h=0.3 - β^*=1	h=0.3 - β^*=-1
4.787	4.777	4.751	4.746	4.748

Table 2 Evaluation of the area(mm^2) under each curve in Fig. 7 as a function of the mesh size h(mm) and β^*(mm^{-2}).

h=0.2 - β^*=1	h=0.2 - β^*=-1	h=0.3 - β^*=0 [5]	h=0.3 - β^*=1	h=0.3 - β^*=-1
-	0.2%	0.75%	0.86%	0.82%

Table 3 Relative difference between areas under each curve in Fig. 7 as a function of the mesh size h(mm) and β^*(mm^{-2}).

4.2 Building of a wall by LMD-p process

A wall is here manufactured with 10 superimposed single deposits of about 200mm long as shown in Fig. 8. A 316L stainless steel is deposited by Laser Metal Deposition in powder form (LMD-p) on a substrate made of the same material with a scanning velocity equal to 16.66mm.s^{-1}. The wall is built by means of a back and forth strategy on a Trumpf TruLaser cell 7040© equipped with a laser TruDisk©Nd. The power of the laser is equal to 4000W.

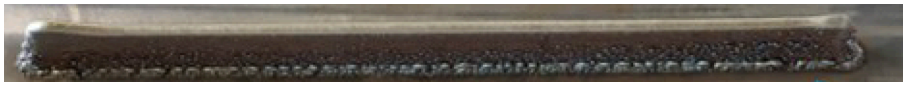

Fig. 8 Wall composed of 10 single beads.

The simulation parameters are the same as the one detailed in Sec. 4.1 for a measured wall width of about 5,3mm (R=2.65mm, Δt=0.01s and ϵ=5%). The mesh size h and the time step Δt are taken equal to 0.3 mm and 0.01s respectively. The deposition trajectory was analyzed with a high speed camera (see Fig. 1) at the start of the bead in order to determine the time delay between the ignition of the molten pool and the start of the nozzle movement. It was estimated to be about 0.1s. This time delay was also observed at the end of the bead between the stopping of the nozzle trajectory and the extinction of the weld bath. From the numerical point of view, this time delay is modeled by means of a nil scanning velocity (see Fig. 1) of the source during 0.1s at the beginning or the end of each bead. The height increment due to each deposition was measured experimentally in the middle of the wall from lateral pictures coming from the camera (see Fig. 1). The experimental values are plotted in Fig. 9.

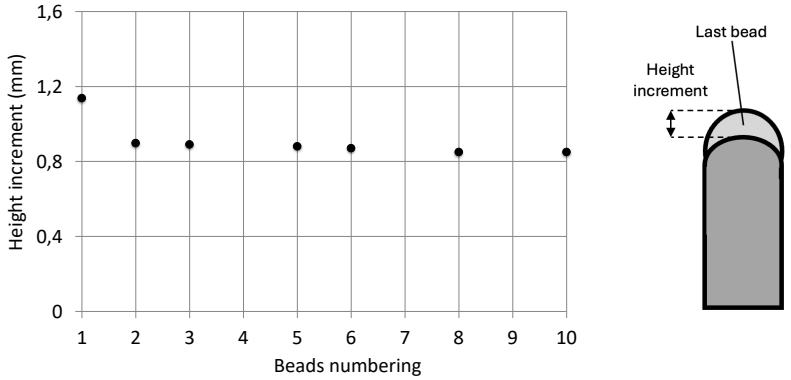

Fig. 9 Experimental height increment after each deposition.

For the simulation developed in section 3, 2 parameters need to be calibrated : β^* and η. In practice, the analysis focuses on $\eta\, q_{max}$ and not η for more convenience. In order to study the influence of these parameters on the geometrical response of the numerical model, 3 first simulations have been carried out considering 3 values for $\eta\, q_{max}$ described in Tab. 4. The chosen values correspond to a range of admissible volume of material added into the molten pool.

	Minimum value	**Mean value**	**Maximum value**
$\eta\, q_{max}$ (mm.s^{-1})	2	3	4

Table 4 Simulated values of $\eta\, q_{max}$.

It is to be noted that experience shows that the numerical method proposed by Feulvarch *et al.* [6] (β^*=0mm^{-2}) is unable to simulate more than 4 depositions. The resolution procedure does not converge regardless of the mesh size and the four first superimposed beads give a wall width significantly lower than the one observed experimentally.

All the simulations have been performed using the software Sysweld® [18]. The remeshing procedure detailed in Sec. 3.3 is applied after the deposition of each of the 10 beads of 200mm long. The CPU time is about 1h for the longest time consuming simulation on a laptop computer (Intel(R) Core(TM) i7-10850H CPU @ 2.70Ghz with RAM of 16 Gb) without considering parallel computing.

Fig. 10 shows the impact of $\eta\, q_{max}$ on the increments of height increase of the wall. One can note that $\eta\, q_{max}$ seems to have a quasi linear influence especially for the last deposits. By using a linear interpolation for the 10^{th} bead, it can be evaluated to about 3.5mm.s^{-1} on Fig. 10 for an experimental height increase of about 0.86mm (see Fig. 9).

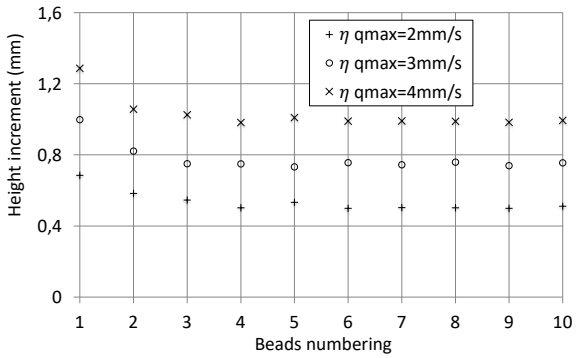

Fig. 10 Numerical height increment after each deposition for β^*=-1mm^{-2}.

By considering the value of $\eta\, q_{max}$ calibrated above, Fig. 11 shows the impact of β^*. It is to be noted that this parameter only influences the height increment of the first 2 deposits, with the same gap. By using a linear interpolation for the 1^{st} bead, β^* can be taken equal to about -1.4mm^{-2} on Fig. 11 for an experimental height increment of about 1,14mm (see Fig. 9).

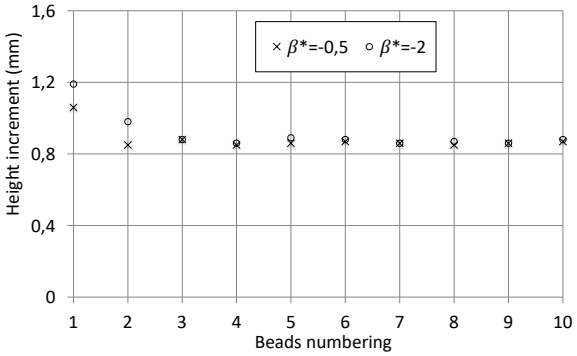

Fig. 11 Numerical height increment after each deposition for $\eta\, q_{max}$=3.5mm.s^{-1} as a function of β^* (mm^{-2}).

The results of the calibrated simulation and the experimental values are plotted in Fig. 12. One can note that the comparison is very satisfactory. Fig. 13 shows the geometry of the wall computed with the numerical method developed. It is important to notice that the time delay of 0.1s at the beginning and stopping of each deposition makes it possible to obtain a vertical geometry at each end of the wall. Without considering this, the numerical wall is oblique as can be observed in reality.

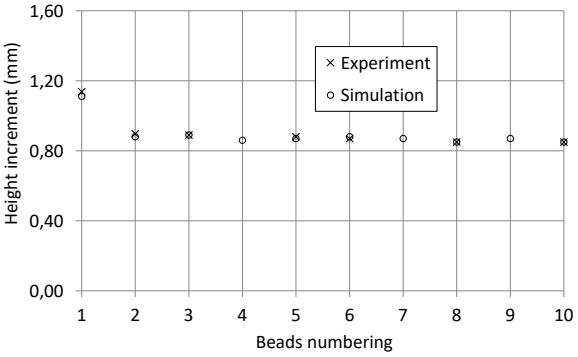

Fig. 12 Experimental and numerical height increment after each deposition ($\eta\, q_{max}$=3.5mm.s^{-1} ; β^*=-1,4mm^{-2}).

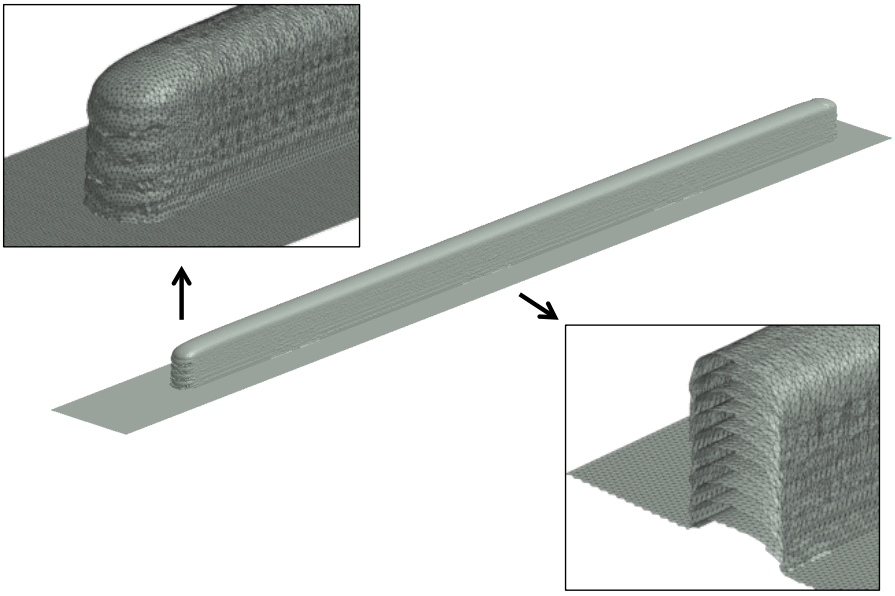

Fig. 13 Computed geometry ($\eta\, q_{max}$=3.5mm.s^{-1} ; β^*=-1,4mm^{-2}) with the successive configurations of the mesh after each deposition.

5 Conclusions

A fast FEM method for simulating beads geometry during direct energy deposition additive manufacturing has been proposed. Such a computational tool can help to study the influence of the sequence of deposition on the geometry in a quick way.

At first, A constant vertical evolution rate of the surface tension is incorporated into the FEM algorithm firstly proposed by Feulvarch *et al.* [6] to adjust the geometry of the free surface of the molten pool which depends on the hydrodynamics induced by buoyancy forces and the Marangoni's effect. The interest of the new approach lies in the fact that it is very fast because it is based on a 2D mesh composed of linear triangles that corresponds to the sole surface of the 3D manufactured component. Moreover, the advantage of the implicit nonlinear resolution algorithm developed lies in the fact that it avoids matrix systems resolution allowing efficient parallel computing. A simple remeshing procedure was also detailed without requiring any field projection. Indeed, the geometry serves as the only historical data required to resume FEM computations following each remeshing step. As an example, it is shown that a wall made of 10 overlapping beads of 200mm long can be simulated with a CPU time of about 1h on a laptop computer.

Future works will focus on the coupling with heat transfer. The objective will be to define the surface of the molten pool from the zone having a temperature higher than the solidus and not by means of a radius R as proposed

in this paper (see Eq. (23)). In this way, it could be possible to numerically optimize the manufacturing strategy anticipating overheating phenomena that can lead to a collapse of the component during additive manufacturing. In the longer term, the objective is to couple the numerical method proposed with the simulation of heat transfer but also the computation of distortions in order to optimize the manufacturing strategy at the scale of a complete component and not only a few beads.

References

1. Rabier S., Medale M. (2003), Computation of free surface flows with a projection FEM in a moving mesh framework, Comput. Methods Appl. Mech. Engrg., **192**, 4703-4721.
2. Yancheng Zhang, Qiang Chen, Gildas Guillemot, Charles-André Gandin, Michel Bellet (2018), Numerical modelling of fluid and solid thermomechanics in additive manufacturing by powder-bed fusion: Continuum and level set formulation applied to track- and part-scale simulations, C. R. Mecanique, **346**, 1055-1071.
3. S. Cadiou, M. Courtois*, M. Carin, W. Berckmans, P. Le masson, 3D heat transfer, fluid flow and electromagnetic model for cold metal transfer wire arc additive manufacturing (Cmt-Waam), Additive Manufacturing 36 (2020) 101541.
4. Saadlaoui Y., Feulvarch E., Delache A., Leblond J.-B., Bergheau J.-M. (2018), A new strategy for the numerical modeling of a weld pool, C. R.Mecanique, **346**, p. 999-1017.
5. Yabo Jia, Yassine Saadlaoui, Eric Feulvarch, Jean-Michel Bergheau, An efficient local moving thermal-fluid framework for accelerating heat and mass transfer simulation during welding and additive manufacturing processes, Computer Methods in Applied Mechanics and Engineering, Volume 419, 1 February 2024, 116673.
6. E. Feulvarch, F. Josse, J.-C. Roux, A. Sova, An efficient reduced-physics-coupling FEM formulation for simulating a molten metal deposition geometry, European Journal of Mechanics / A Solids 89 (2021) 104290.
7. Leblond J.-B., Amin El Sayed H., Bergheau J.-M. (2013). On the incorporation of surface tension in finite-element calculations, C. R. Mecanique, **341**, p.770-775.
8. Bellet M., Implementation of surface tension with wall adhesion effects in a three-dimensional finite element model for fluid flow, Commun. Numer. Methods Eng. 17 (2001) 563-579.
9. Ruschak K.J., A method for incorporating free surface boundaries with surface tension in finite element fluid-flow simulators, Int. J. Numer. Methods Eng. 15 (1980) 639-648.
10. Bach P., Hassager O., An algorithm for the use of the Lagrangian specification in Newtonian fluid mechanics with applications to free surface fluid flow, J. Fluid Mech. 152 (1985) 173-190.
11. Christodoulou K.N., Scriven L.E., The fluid mechanics of slide coating, J. Fluid Mech. 208 (1989) 321-354.
12. Cairncross R.A. , Schunk P.R., Baer T.A., Bao R.R., Sackinger P.A., Finite element method for free surface flows of incompressible fluids in three dimensions. PartI. Boundary fitted mesh motion, Int. J. Numer. Methods Fluids 33 (2000) 375-403.
13. Feulvarch E., Bergheau J.-M., Leblond J.-B. (2009), An implicit finite element algorithm for the simulation of diffusion with phase changes in solids, Int. J. Numer. Meth. Engng, **78**, p. 1492-1512.
14. Ciarlet Ph, Segal A. The Finite Element Method for Elliptic Problems. North-Holland: Amsterdam, 1978.
15. Rassineux, A., Villon, P., Savignat, J.-M., Stab, O., Surface remeshing by local hermite diffuse interpolation, (2000) International Journal for Numerical Methods in Engineering, 49 (1-2), pp. 31-49.
16. Lorensen, W. E., Cline, H. E. (1987). Marching cubes: A high resolution 3D surface construction algorithm. ACM SIGGRAPH Computer Graphics, 21(4), 163-169.
17. Rassineux, A. (2021). Robust conformal adaptive meshing of complex textile composites unit cells. Composite Structures, 114740, DOI: 10.1016/j.compstruct.2021.114740
18. ESI Group, Users Manual, 2024.